Received: 22 February 2023 | Revised: 2 March 2023 | Accepted: 7 March 2023

DOI: 10.1002/cey2.371

RESEARCH ARTICLE

CARBON ENERGY WILEY

Pressureless all-solid-state Na/S batteries with self-supporting $Na_5YSi_4O_{12}$ scaffolds

Aikai Yang[1,2] | **Ruijie Ye**[1] | **Huimin Song**[3] | **Qiongqiong Lu**[4,5] | **Xingchao Wang**[6] | **Enkhtsetseg Dashjav**[1] | **Kai Yao**[1] | **Daniel Grüner**[7] | **Qianli Ma**[1] | **Frank Tietz**[1] | **Olivier Guillon**[1,2,8]

[1]Forschungszentrum Jülich GmbH, Institute of Energy and Climate Research (IEK-1), Jülich, Germany

[2]Institute of Mineral Engineering (GHI), RWTH Aachen University, Aachen, Germany

[3]Beijing Key Laboratory of Theory and Technology for Advanced Batteries Materials, School of Materials Science and Engineering, Peking University, Beijing, China

[4]Institute of Materials, Henan Academy of Sciences, Zhengzhou, Henan, China

[5]Henan Key Laboratory of Advanced Conductor Materials, Zhengzhou, Henan, China

[6]State Key Laboratory of Chemistry and Utilization of Carbon Based Energy Resources, Key Laboratory of Advanced Functional Materials, Autonomous Region, Institute of Applied Chemistry, College of Chemistry, Xinjiang University, Urumqi, Xinjiang, China

[7]Forschungszentrum Jülich GmbH, Institute of Energy and Climate Research (IEK-2), Jülich, Germany

[8]Jülich Aachen Research Alliance, JARA-Energy, Jülich, Germany

Correspondence
Frank Tietz, Forschungszentrum Jülich GmbH, Institute of Energy and Climate Research (IEK-1), Jülich 52425, Germany.
Email: f.tietz@fz-juelich.de

Funding information
China Scholarship Council, Grant/Award Number: 201906200023; Bundesministerium für Forschung und Technologie, Grant/Award Number: 13XP0390B

Abstract

The development of reliable and affordable all-solid-state sodium metal batteries (ASS-SMBs) requires suitable solid-state electrolytes with cost-efficient processing and stabilized electrode/electrolyte interfaces. Here, an integrated porous/dense/porous $Na_5YSi_4O_{12}$ (NYS) trilayered scaffold is designed and fabricated by tape casting using aqueous slurries. In this template-based NYS scaffold, the dense layer in the middle serves as a separator and the porous layers on both sides accommodate the active materials with their volume changes during the charge/discharge processes, increasing the contact area and thus enhancing the utilization rate and homogenizing the current distribution. The Na/NYS/Na symmetric cells with the Pb-coated NYS scaffold exhibit significantly reduced interfacial impedance and superior critical current density of up to 3.0 mA cm^{-2} against Na metal owing to enhanced wettability. Furthermore, the assembled Na/NYS/S full cells operated without external pressure at room temperature showed a high initial discharge capacity of 970 mAh g^{-1} and good cycling stability with a capacity of 600 mAh g^{-1} after 150 cycles (based on the mass of sulfur). This approach

paves the way for the realization of economical and practical ASS-SMBs from the perspective of ceramic manufacturing.

KEYWORDS

Na/S batteries, $Na_5YSi_4O_{12}$, scaffold, solid-state electrolytes, tape casting

1 | INTRODUCTION

Lithium-ion batteries (LIBs) play a pivotal role in portable electronics and electromobility due to their superior specific energy and excellent cycling performance.[1,2] However, with the substantial consumption of lithium resources and critical cathode materials, including nickel, cobalt, and other metals, the cost and environmental impact of resources used for LIBs are soaring during recent years.[3–5] In addition, batteries, as energy storage devices for the interconversion between electrical and chemical energy, play a crucial role in the utilization of intermittent energy sources by delivering stabilized voltage and shifting peak load.[6–8] Compared to conventional LIBs, the all-solid-state sodium metal batteries (ASS-SMBs) could provide an ecologically friendlier alternative in the grid-scale energy storage market.[9–13]

There is no doubt that solid-state electrolytes (SSEs) with high ionic conductivity and chemical stability are the essential components of solid-state batteries (SSBs).[14–16] Since the discovery of the Na^+ ion conductivity in β-Al_2O_3,[17] Li^+ and Na^+ ionic transport has been identified in oxides, sulfides, and polymers and has strongly triggered the research in the field of solid-state ionics.[18–28] As early as the 1960s, high-temperature Na/S and $Na/NiCl_2$ batteries using Na^+ ionic conductors such as β/β''-Al_2O_3 as separators have been designed and commercialized for large-scale energy storage.[29–31] However, these high-temperature batteries with liquid electrodes usually have limited energy efficiency and give rise to high safety concerns.[32] Therefore, the development of room-temperature (RT) Na^+ ionic conductors and safer sodium batteries such as SSBs is of great significance.[33–35] Nonetheless, SSBs operating at RT usually suffer from a very high interfacial impedance due to the poor solid–solid contact at the interfaces between the SSE and both electrodes.[36–38] Furthermore, maintaining a stable interface and good contact is also challenging due to the considerable volume changes of active materials, resulting from repeated electrochemical reactions in the electrodes.[39,40] The deterioration of interfaces can consequently induce dendrite formation in the anode compartment and underutilize active materials in the cathode, hence causing battery degradation or even failure.[37,41,42] In practice, various strategies are applied to avoid the battery fading of SSBs. For example, the application of external stacking pressure, cosintering of composite electrodes, and modification of interfaces are required to ensure stable interfaces.[35,43–45]

Recently, silicate-based $Na_5YSi_4O_{12}$ (NYS) Na^+ superionic conductor sheets were fabricated by our group[46] using the well-established tape casting technique. They exhibit good RT conductivity (1 mS cm^{-1}) and a wide electrochemical stability window (>8 V vs. Na^+/Na). However, some challenges still exist related to the utilization of NYS sheets in SSBs: the fabrication of thin but robust electrolytes, the construction of stable electrode/electrolyte interfaces, and the selection of compatible cathodes.[47,48] To tackle the aforementioned challenges, the well-established aqueous tape casting technique is employed to fabricate a porous/dense/porous NYS trilayered structure with scaffolds for the electrode materials. The NYS layers with a total thickness of 300–400 μm provide the necessary ionic conductivity and stability, whereby the dense layer in the middle separates both electrodes and the porous layers on both sides accommodate the active materials. With high capacity and low-cost advantages, elemental sulfur is used as the cathode active material of choice[49] and coupled with a Na metal anode to create a Na/NYS/S battery that can operate at RT. The half- and overall-cell reactions are as follows[50]:

$$\text{Negative electrode: } x\text{Na} \leftrightarrow x\text{Na}^+ + xe^-, \quad (1)$$

$$\text{Positive electrode: S} + x\text{Na}^+ + xe^- \leftrightarrow \text{Na}_x\text{S}, \quad (2)$$

$$\text{Overall: S} + x\text{Na} \leftrightarrow \text{Na}_x\text{S}(0 \le x \le 2), \quad (3)$$

where the theoretical capacity (C_{th}) of 1675 mAh g_S^{-1} is based on the fully sodiated state (Na_2S).[51,52] In the following, the capacity is referred to the weight of sulfur (g_S^{-1}). In conventional Na/S batteries with liquid electrolytes, S and polysulfides dissolve into the electrolyte and then shuttle to the Na metal anode, resulting in a severe self-discharge behavior and continuous capacity degradation of the batteries.[49,53–55] Furthermore, S as the cathode active material usually undergoes severe volume changes during charge and discharge so that the S electrode sheets manufactured by typical coating

processing detach from the current collector inducing irreversible capacity loss.[51] In contrast, the dense NYS layer used here effectively prevents the shuttling of S and the open porosity present in the NYS scaffold additionally provides space for the volume swelling of S during sodiation while increasing the contact area between S and NYS electrolytes. For the infiltrated Na metal anode, the NYS porous structure can be coated with Pb to effectively improve the interfacial wettability between Na and NYS.[56] This reduces the interfacial impedance, increases the contact area, and distributes the local current.

Therefore, the main benefits of the porous/dense/porous NYS trilayered scaffold structure fabricated by aqueous tape casting are as follows: (1) stable interfaces between the electrode active materials and the NYS electrolyte enable pressureless Na/NYS/Na symmetric cells and Na/NYS/S full cells with good cycling stability; (2) the porous structure provides a host for the S composite cathode while increasing the contact area and improving the utilization rate; (3) the thin Pb-coating of the porous NYS scaffold effectively improves its wettability with the Na metal[56] and distributes the local current; and (4) the aqueous tape casting process used for the fabrication of NYS ceramics is eco-friendly and has the potential for scale-up. This work presents a promising design for pressureless ceramic-based Na/S batteries and provides a new paradigm for the development of cheap and reliable ASS-SMBs. It also shows for the first time the application of NYS in a realistic cell design beyond the generic use of ceramic pellets.[41,57]

2 | EXPERIMENTAL SECTION

2.1 | Fabrication and synthesis

Preparation of $Na_5YSi_4O_{12}$ precursor for tape casting: The raw materials $Na_2CO_3{\cdot}H_2O$ (99%; Aldrich), Y_2O_3 (99.999%; VWR), and SiO_2 (99%, 1–5 μm; Honeywell Fluka) were mixed in a stoichiometric ratio and milled with ZrO_2 balls (3 and 5 mm in diameter, 200 rpm) and ethanol as a dispersant for 24 h. After ball-milling, the mixture of raw materials was heated in an oven (60°C for 24 h) in flowing N_2. The white powder was calcined at 950°C for 5 h in air. Then, the calcined powder was roughly ground in an agate mortar and subsequently ball-milled for 24 h to decrease the particle size of the NYS precursor for the subsequent fabrication of the NYS tape. Part of the NYS precursor was sintered at 1100°C for 6 h in air to obtain the pure NYS phase and then ball-milled to obtain fine particle sizes as an additive in the S composite cathode.

Fabrication of porous and dense NYS tapes: The aqueous slurry for dense and porous tapes was prepared by mixing methylcellulose (Alfa Aesar), polyethylene glycol (Merck), and glycerol (99%; Merck) in deionized water with the assistance of a stirrer (IKA, RET Basic). Then, the finely ground NYS precursor powder was added to the slurry. For the preparation of the porous tape, spherical polymethylmethacrylate (PMMA; Merck) particles with an average diameter of 100 μm were admixed to the slurry acting as a pore former. Both suspensions for dense and porous layers were homogenized in vacuum (~10^4 Pa) with ZrO_2 balls (5 mm in diameter) in a planetary mixer (ARE-500; Thinky) at 1000 rpm for 10 min to form uniform slurries for the subsequent casting step. The mixed slurries were individually transferred to the slurry reservoir of the tape-casting machine and then cast on a Mylar substrate using a height-adjustable doctor blade. A slit width of 400 μm in thickness and 10 mm s^{-1} casting speed was applied. After drying naturally at RT overnight, the dense and porous green tapes were easily peeled off from the Mylar substrate. The obtained green tapes were thin and flexible and could be punched into the desired round-shaped samples with varying diameters and laminated into multilayer structures. Each piece of tape was first pressed with 60 MPa at RT for 2 min to improve the green density, which can break and flatten the PMMA spheres in the porous tapes to some extent. Then, these pressed tapes were laminated together to obtain the porous/dense/porous trilayered structure by subsequent warm pressing at 80°C with 120 MPa for 2 min. Finally, the laminated tapes were sintered in air with a heating rate of 60°C h^{-1} until 600°C for 1 h to decompose the organic additives, followed by a heating rate of 180°C h^{-1} up to 1100°C for 6 h to densify the tapes. During sintering, the green tapes were placed between two sintered NYS pellets prepared with the same raw powder. This prevented the tapes from bending into a bowl shape and sticking to the substrate during the sintering process.

Preparation of S composite cathode paste: polyvinylidenfluorid (M_w = 600,000; Sigma-Aldrich) powder was dissolved in *N*-methyl-2-pyrrolidone (NMP; Merck) under magnetic stirring (IKA, RET Basic). The polyethylene oxide (PEO) (M_w = 200,000; Alfa Aesar) powder was added to acetonitrile (Merck) and agitated until completely dissolved. The anhydrous $NaClO_4$ powder (Alfa Aesar) was then added to the PEO solution with the molar ratio of EO:Na^+ = 10:1. Both solutions were mixed together and stirred until homogeneity was achieved. The elemental sulfur powder (Alfa Aesar) as the active material, the carbon black of super P (Alfa Aesar) as the electronic conductor, and NYS powder with pure phase as the bifunctional plasticizer to decrease the crystallinity of PEO chains and increase the Na^+ ionic

conductivity were added into the solution and mixed with stirring for 6 h to get a uniform and concentrated paste. Different weight fractions of S (20, 32, 40, 50, 60 wt%) in the composite cathode were fabricated (see Table S6). The last step was homogenization in a high-speed mixer device (ARE-500, 1500 rpm for 10 minutes; Thinky) to completely mix the paste.

Fabrication of symmetric and full cells: (1) For the Na/NYS/Na symmetric cells, both porous sides of the NYS scaffold were sputter-coated with a Pb layer (Pb target: micro to nano, 70-PB5708; Cressington Sputter Coater 108 Auto Series) to ameliorate the wettability between the Na metal and NYS ceramic. The Pb layer was sputtered at a current of 20 mA for 120 s, which gives rise to a uniform Pb coating with a thickness of 50 nm. The weight ratio of Pb in the Na anode side is about 5 wt% (0.1 mg Pb and 2.0 mg Na). The diameter of the sintered NYS scaffold varied between 10 and 14 mm (usually 12 mm). The Na metal was heated to melt (120–150°C) in a glass bottle, and then the liquid Na metal was pipetted and dropped on both sides of the Pb-coated NYS scaffold. The melting and dropping of the Na metal were conducted in an Ar-filled glovebox ($p(O_2) < 1.0$ ppm and $p(H_2O) < 0.5$ ppm; Glovebox System). Once the Na metal had solidified, the Al foils (0.01 mm in thickness; Dezhi Company) were attached on both sides as current collectors and mounted in a pouch cell with an aluminum-plastic film (Dezhi Company) and sealed in the glovebox. (2) For the assembly of the full cells, one side of the NYS scaffold was coated with a Pb layer to accommodate the Na metal as an anode. The other side filled with the prepared S composite cathode paste was poured and gently squeezed into the porous layer. An excess of paste was gently scraped off. The filled scaffold was dried naturally (48 h) in a ventilated hood to remove the solvents. The areal loading of S was calculated from the mass difference before coating and after complete drying, which is usually in the range of 0.9–1.0 mg cm^{-2}. The procedure of loading the Na anode was the same as in the case of symmetric cells.

2.2 | Characterization

2.2.1 | Crystal structure characterization

The crystal structure of the as-prepared NYS scaffold was determined by X-ray diffraction (XRD; Bruker D4 Endeavor) with Cu K_α radiation. The refinement of the XRD pattern was carried out with Fullprof Suite software to get the detailed lattice parameters of the unit cell. The XRD sample was NYS powder, which was ground in an agate mortar from the as-sintered NYS trilayer.

2.2.2 | Morphological characterization

The microstructure of the NYS scaffold was analyzed with scanning electron microscopy (Hitachi TM3000). The NYS scaffold was coated with a thin Au layer to improve electrical contact before being transferred to the sample chamber.

The pore volume of the porous layer in the NYS scaffold was determined with Archimedes' method. The sintered NYS scaffold was immersed in liquid propanol for 24 h and then weighed after removing the propanol residuals on the surface. The density of propanol at RT was 0.8034 g cm^{-3}.

2.2.3 | Particle size measurement

The particle size measurement was conducted with a laser-scattering particle size distribution analyzer (LA-950; HORIBA). The particle size distribution of the NYS precursor powder after calcination is shown in Figure S7.

2.2.4 | Electrochemical measurements

All electrochemical performance tests were performed with an electrochemical workstation (BioLogic VMP300) equipped with climate chambers (VT4002; Vötsch) to adjust the temperature. The a.c. impedance measurements of the Na/NYS/Na symmetric cells were performed in the frequency range from 7 MHz to 1 Hz with an alternating voltage amplitude of 5 mV. The fitting of the impedance data was carried out with Zview software (Scribner Associates Inc.). The temperature-dependent impedance spectra were recorded between −20°C and 80°C and then plotted in an Arrhenius diagram to determine the activation energy (E_a) of Na^+ ionic conduction. The critical current density (CCD) was measured with Na/NYS/Na symmetric cells by gradually increasing the current density at RT. The cycling stability of the Na/NYS/Na cells was measured with galvanostatic cycling at 1.3 mA cm^{-2} and 1.3 mAh cm^{-2}. The signals occurring during cyclic voltammetry (CV) were recorded between −0.5 and 8 V (vs. Na^+/Na) with a scanning rate of 0.01 mV s^{-1} to obtain the electrochemical window of the Au/NYS/Na cell (Au as the cathode and Na as the anode), in which the Au was coated with a sputter coater device (20 mA applied current; 150 s coating time). The long-term galvanostatic charge and discharge performance of the Na/NYS/S full cells were tested in the voltage range of 1.0–3.3 V versus Na^+/Na, whereas 3.5 V was applied for the test at different current

densities (from 0.017 to 3.4 mA cm^{-2}. The impedance spectra of the full cell were measured with the same setting as in the case of the symmetric cells. The CV curves at the different scanning rates from 0.01 to 100 mV s^{-1} were recorded in the range of 1.0–3.5 V vs. Na^+/Na. The electronic conductivity of the composite cathode was characterized using Ni/composite cathode/Ni symmetric cells by applying a constant voltage of 0.1 V and recording the current. The electronic conductivity can be calculated according to Ohm's law using the constant current value. The Na^+ ionic conductivity of the composite cathode was measured with symmetric cells composed of NYS dense tape/composite cathode/NYS dense tape. The NYS dense layers act as Na^+ ion reversible electrodes and electronically blocking electrodes to eliminate the contribution of electronic conduction.

3 | RESULTS AND DISCUSSION

3.1 | Fabrication, microscopic, and crystal structure of NYS trilayer

The NYS precursor was prepared using a ball-milling process followed by heat treatment, as shown in Figure 1A. For the following tape casting, the NYS precursor was mixed with the binder and plasticizer. The porous layers required the addition of a pore former. Here, spherical polymethylmethacrylate (PMMA) beads were used to prepare the porous layers. The NYS and NYS/PMMA green tapes were laminated together before cosintering. The slurry preparation and the sintering protocol followed the preparation of dense tapes of NYS.[46] The microstructure (Figure 1B) of the sintered tapes shows that the dense and porous layers are very tightly joined, which facilitates the rapid migration of Na^+ ions in the NYS phase and results in a robust mechanical scaffold with good flatness due to the symmetric geometry of the laminates. The thicknesses of the dense and porous layers were 90 and 170 μm after sintering, respectively. The dense layer (Figure 1C) can effectively support the entire trilayered laminate and separates both electrodes due to the high hardness (2 GPa) and elastic modulus (45 GPa), which is sufficient to maintain excellent mechanical properties during cycling.[46] The micron-scale interconnected open pores in the porous layer (Figure 1D) can accommodate electrode active materials and simultaneously provide continuous Na^+ ionic transport pathways. The pore volume in the porous layer is about 68% as determined by Archimedes' method and very suitable for infiltration. The NYS phase crystallized in rhombohedral symmetry with a space group of $R\bar{3}c$, which is revealed by the XRD pattern (Figure 1E) and Rietveld refinement (refined parameters of the unit cell shown in Figure 1F are listed in Table S1). An explanation for the appearance of secondary phases is described in Note S1 at the end of the Supporting Information.

3.2 | Electrochemical performance of Na/NYS/Na symmetric cells

The as-prepared NYS scaffold was used to assemble Na/NYS/Na symmetric cells to evaluate Na^+ ionic conductivity with impedance spectroscopy. Different from the determination of the electrode area of dense NYS tapes, the precise contact area between the Na metal and electrolyte and the influence of tortuosity in the porous layers are difficult to be analyzed. As a simplified approach to obtain comparable values of conductivity, the total thickness of the NYS scaffold and the planar area based on the tape diameter are used for the calculation of conductivity. The total ionic conductivity σ_{total} (sum of conductivities of bulk and grain boundaries) of the NYS scaffold is 1.0 mS cm^{-1} at RT, which corresponds to the first semicircle in the fitted impedance spectra (Figure 2A,B). The values of the individual components of the fitted impedance spectra are listed in Table S2. The area-specific resistance (ASR) of the NYS trilayer is only 43 Ω cm^2 based on the following equation[36]:

$$\mathrm{ASR} = \frac{l}{\sigma}, \tag{4}$$

where l is the thickness and σ is the conductivity of the electrolyte. For the pristine NYS scaffold in the symmetric cell, the interfacial resistance ($R_{interface}$) is as high as 5000 Ω cm^2 (Figure 2A) derived from the second semicircle in the fitted impedance spectrum. In contrast, the $R_{interface}$ is reduced to 25 Ω cm^2 (Figure 2B) for the Pb-coated NYS scaffold. This is attributed to the significantly improved interfacial wettability of the Na metal on the Pb-coated NYS,[56,58] which was confirmed by the contact angle test (Figure 2C). The Pb coating on the NYS reduces the initial contact angle between the Na metal and NYS from 109° to 41°. In the analogous Na/Pb-coated NYS/Na symmetric cell, the temperature-dependent total conductivity is plotted in an Arrhenius diagram (Figure 2D), and the fitted activation energy (E_a) for Na^+ ion conduction is 0.29 eV, the same value as previously reported.[46]

The CCD at RT is measured by gradually increasing the current density in a symmetric cell until the

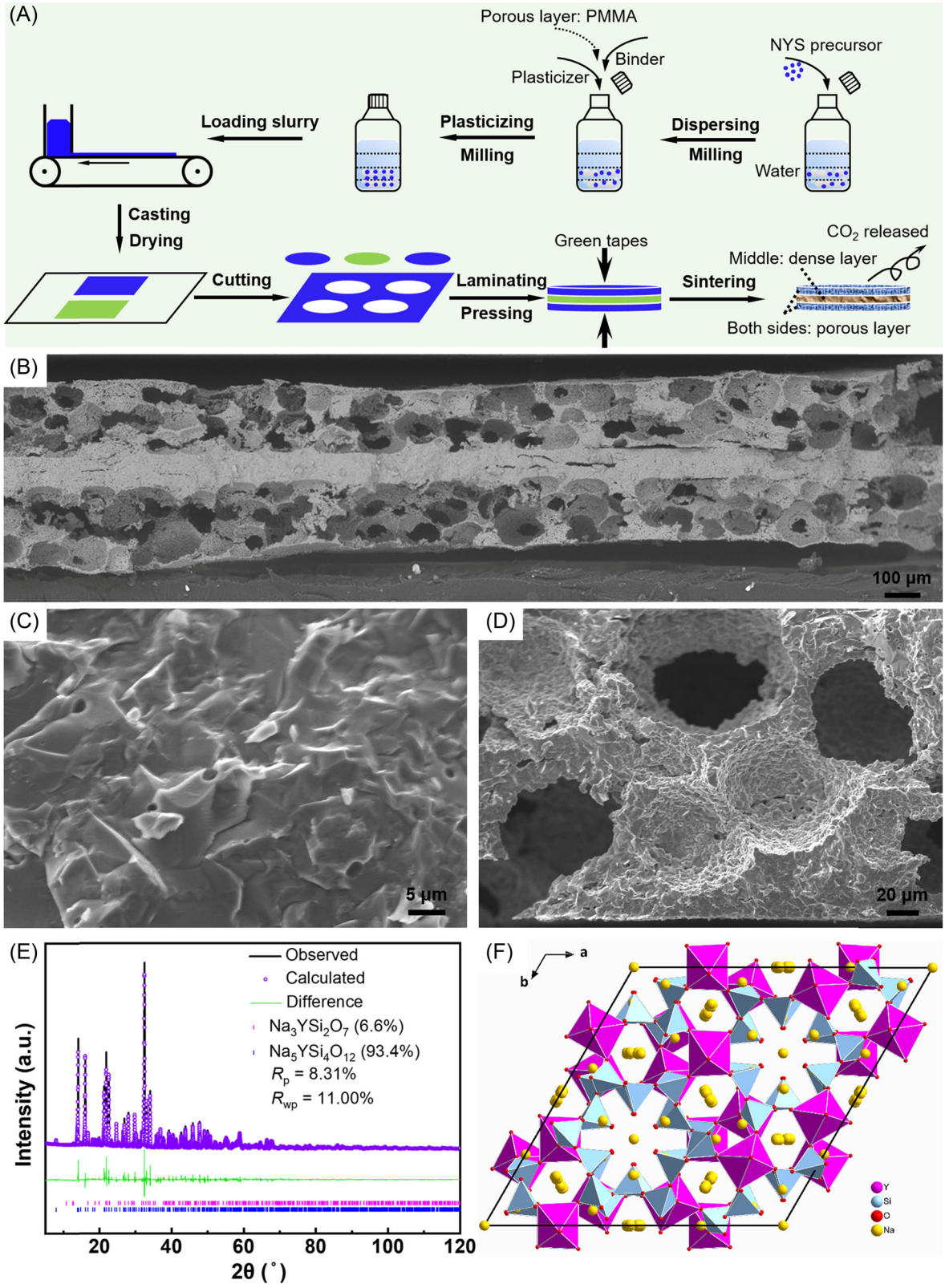

FIGURE 1 (A) Schematic processing steps of the preparation of NYS trilayers: milling of the raw materials, casting the slurries, drying, cutting, laminating, pressing, and sintering the green tapes, (B) cross-sectional SEM image of the NYS trilayered structure, (C, D) magnified SEM images of dense and porous layers, respectively, (E) refined XRD pattern after tape casting and sintering, and (F) projection of crystal structure along the *c*-axis.

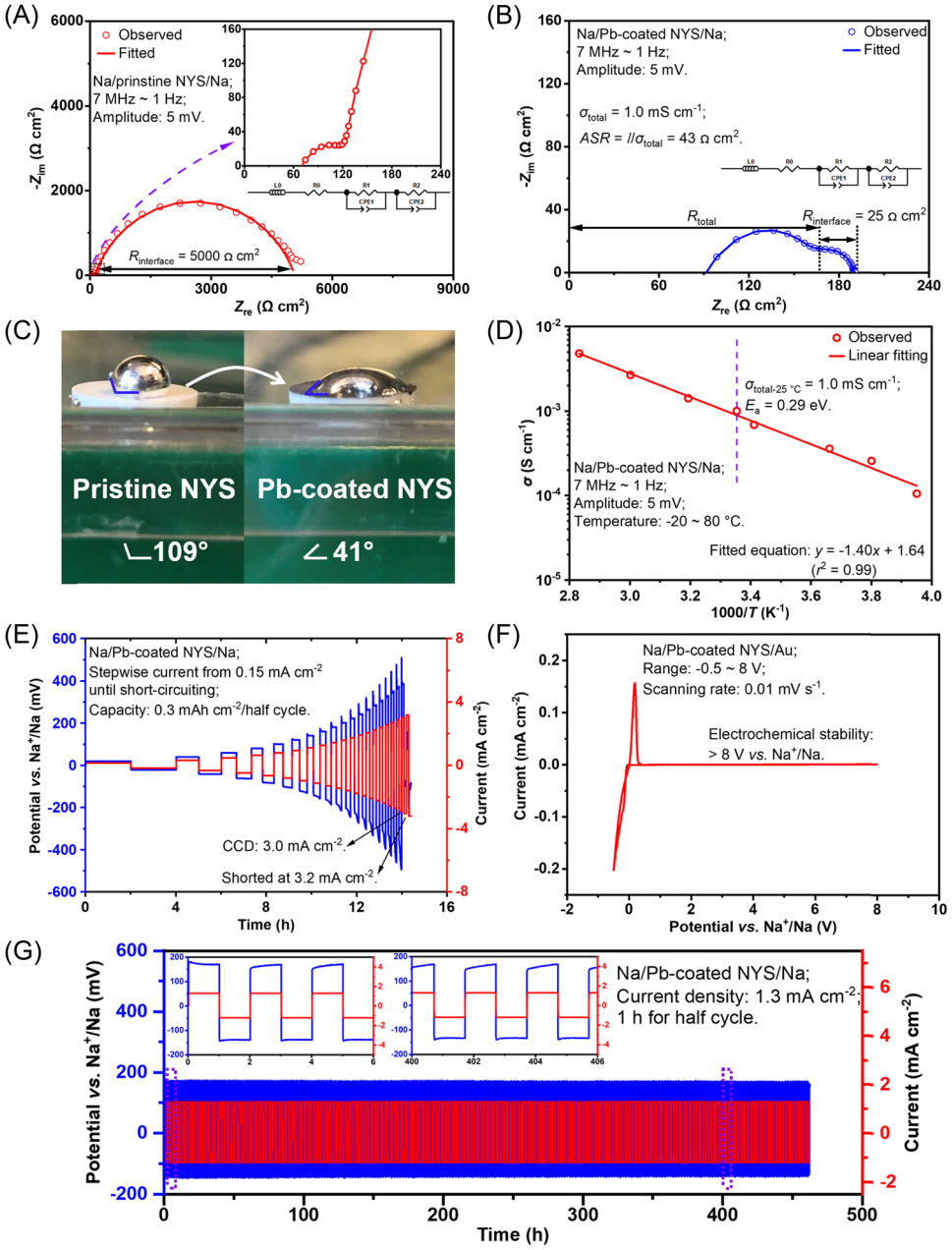

FIGURE 2 Electrochemical performance of the NYS scaffold in Na/NYS/Na symmetric cells and Na/NYS/Au cells. Nyquist plots of the Na/NYS/Na cell with (A) pristine NYS scaffold and (B) Pb-coated NYS scaffold. Insets show the magnified spectrum at high frequencies and the equivalent circuit for fitting. (C) Contact angle measurement for the pristine and Pb-coated NYS scaffold with the Na metal in the glovebox. (D) Arrhenius plot of the temperature-dependent conductivities in the Na/NYS/Na symmetric cell with linear fitting between −20°C and 80°C. (E) CCD measurement with a stepwise increase of the current density until short-circuiting. (F) CV profile in the range of −0.5 to 8 V versus Na^+/Na in the Na/NYS/Au cell with a scanning rate of 0.01 mV s^{-1}. (G) Galvanostatic cycling performance of the Na/NYS/Na symmetric cell at the current density of 1.3 mA cm^{-2} and capacity of 1.3 mAh cm^{-2}. Insets show the magnified profiles in the time intervals of 0–6 and 400–406 h.

polarization voltage significantly fluctuates and the cell is short-circuited. The CCD in Na/NYS/Na symmetric cells with the NYS scaffold is 3.0 mA cm^{-2} (Figure 2E) against the Na metal, which is higher than those of the previously reported CCD with dense NYS tapes[46] and sheets[57] (both are 2.2 mA cm^{-2}). This is attributed to the good ionic conductivity and the increased contact area in the Pb-coated NYS scaffold. However, an increasing voltage spike occurs starting at the current density of 1.3 mA cm^{-2}, which can be explained by the rate of Na^+ ion transport in the vicinity of the Na/NYS interface. At low current density (<1.3 mA cm^{-2}), the rate of Na^+ ion

depletion is lower than the Na metal diffusion at the stripping side. This leads to low Na vacancy concentration at the interface and maintains good contact, and there is no significant irregular voltage signal. However, when the current density increases, the Na metal diffusion cannot compete with the Na^+ ion depletion, leading to vacancy clustering and void formation at the interface, which causes a sharp voltage increment at the beginning of each cycle. When stripping and plating are reversed, the polarization voltage increases gradually with the return transport of the deposited Na metal and here voids also appear near the interface. Therefore, in the high current density region, the polarization voltages of the first half cycle and the second half circle show opposite trends.

The electrochemical stability window of stripping/plating for Na^+ ions was tested by CV in Na/NYS/Au cells (Figure 2F), showing a wide stability range of over 8 V (vs. Na^+/Na). The sharp redox peaks between −0.5 and 0.5 V versus Na^+/Na suggest no visible side reactions between the Na metal and NYS and high reversibility. The galvanostatic stability indicates that the NYS scaffold easily sustains 460 h cycling (Figure 2G) at a current density of 1.3 mA cm^{-2} and a capacity of 1.3 mAh cm^{-2} without obvious fluctuation of the voltage. This cycling stability is better than that of the reported NYS dense tapes[46] resulting from the increased contact area and improved interfacial wettability between Na and the NYS scaffold. Furthermore, a cycling stability test at 2.4 mA cm^{-2} and 2.4 mAh cm^{-2} (Figure S1) was also conducted to show its practical viability at higher current density, but cycling failed after the 15th cycle. The potential curve is not as stable as that at a lower current density (1.3 mA cm^{-2}) and the obvious voltage fluctuation after the 15th cycle can be explained by the increased amount of the Na metal involved in the plating/stripping processes and the increased tendency of void formation at the interface.

3.3 | Electrochemical performance of the Na/NYS/S full cells

As in a Na/NYS/Na symmetric cell, where the molten Na metal was infused into the porous layer, the composite S cathode paste was squeezed into the porous layer and dried to remove the solvent. Considering the very poor electronic and ionic conductivity of S, the S content was optimized by changing the ratio of conducting additives and S in the composite cathode. The performance of the composite cathode with different S contents was evaluated by measurements of electronic conductivity (Figure S2), ionic conductivity (Figure S3), and specific discharge capacity (Figure S4). The results are summarized in Table S3. By increasing the mass of S in the composite cathode, the electronic conducting additive (super P) and ionic conducting additives (PEO + $NaClO_4$ + NYS) were decreased correspondingly. The trade-off between the conductive additives and the S content revealed that a cathode with 32 wt% showed optimal performance. The XRD patterns with different S contents (Figure S5) further indicate that the crystallinity of PEO in the composite cathode increased with a higher S content, which is unfavorable for Na^+ ionic conduction in the composite cathode.

In the Na/NYS/S full cell, the galvanostatic discharge/charge measurement (Figure 3A) at a current density of 0.017 mA cm^{-2} (equivalent to 0.01 C) with a cathode loading of 1.0 mg cm^{-2} shows that the highest discharge capacity is 970 mAh g_S^{-1} (based on the mass of S, equivalent to the areal capacity of 1.0 mAh cm^{-2}), which is 42% lower than the C_{th} of S. The lower specific discharge capacity reflects the fact that part of the S in the composite cathode is either not sufficiently accessed to be electrochemically active or not completely reduced to Na_2S.[59] The impedance spectra of the full cell at open-circuit voltage (OCV) indicate that the $R_{interface}$ are 94.0 and 327.6 Ω cm^2 (Figure 3B) resulting in a total resistance of the full cell of 500 Ω cm^2. The $R_{interface}$ of the cathode side of the full cell is also evidenced by the high overpotential in Figure 3A,C,D. There are two discharge plateaus, located at ~2.5 and ~2.2 V (vs. Na^+/Na), and the latter region contributes to the majority of the capacity with a relatively smooth voltage decrease. The higher discharge potential vanishes with increasing cycle numbers. During the charging process, there are also two visible plateaus at 2.4 and 2.7 V (vs. Na^+/Na, mean voltage), and the latter charge voltage increases toward 2.9 V with an increasing number of cycles. The multiple discharge/charge plateaus indicate a stepwise reaction of S in the Na/NYS/S full cells.

To analyze the equilibrium potential of the full cell from a thermodynamic perspective, the differential capacitance curve (dQ/dU vs. U; Figure 3C) was plotted. It shows that the equilibrium potentials of the charging and discharging states are 2.32 and 2.21 V, respectively. This is also evidenced by the CV curve of the full cell (Figure 3D). The oxidation (i.e., charge process) peak occurs at around 2.47 V (vs. Na^+/Na) and the reduction (i.e., discharge process) peak at around 2.05 V (vs. Na^+/Na). The polarization voltage of 0.42 V between the charging and discharging process results from the kinetic barriers for the migration of Na^+ ions and electrons at the interfaces in the composite cathode.[60,61]

To study the kinetics of the S composite in the discharge and charge processes, CV curves were recorded

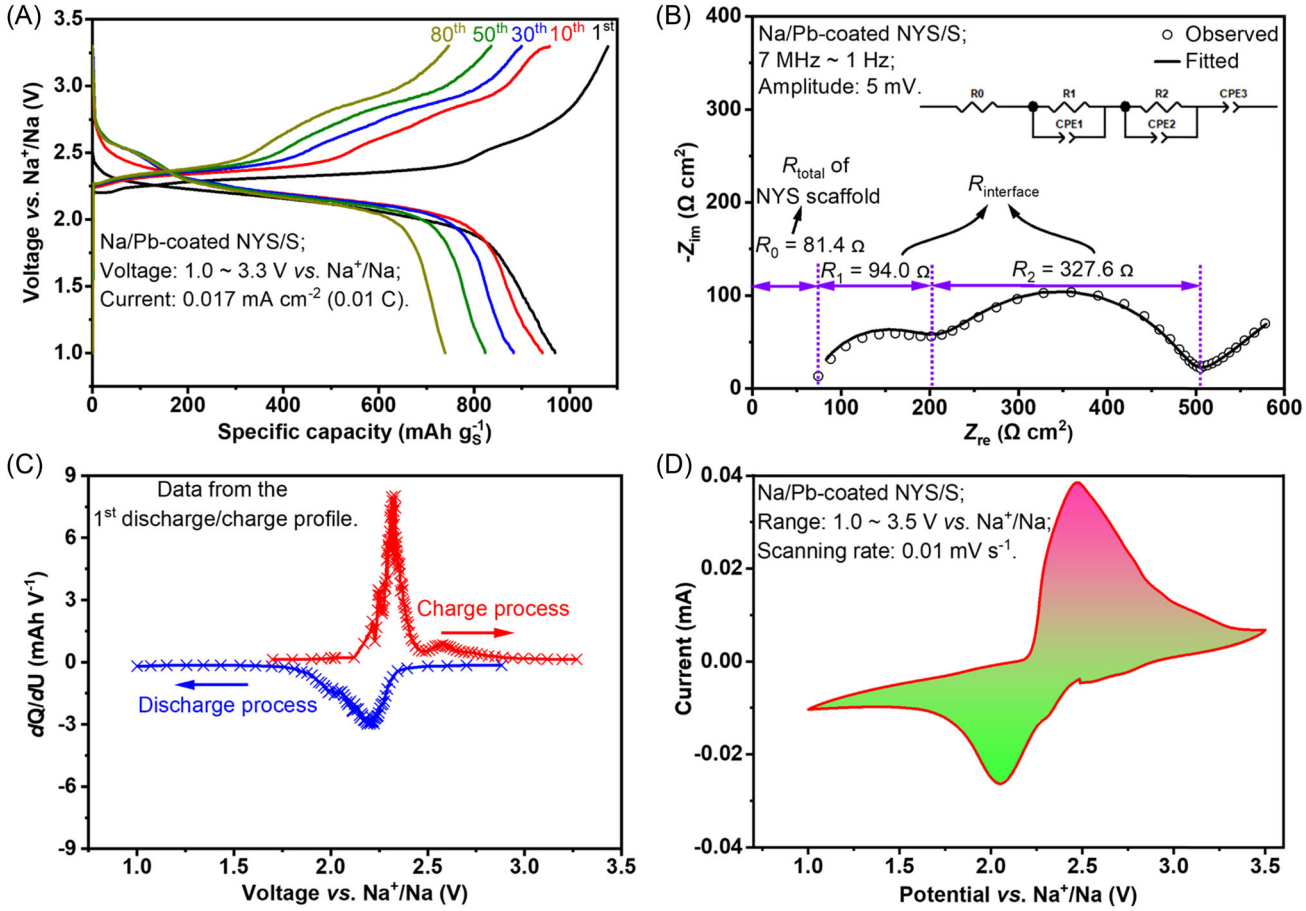

FIGURE 3 Electrochemical performance of Na/NYS/S full cells. (A) Galvanostatic discharge and charge profiles at a rate of 0.01 C in the range of 1–3.3 V versus Na^+/Na. (B) Impedance spectrum of the full cell. The inset shows the equivalent circuit for data fitting. (C) Differential capacity curve from the first discharge and charge profile in (A). *Q* and *U* denote capacity and voltage, respectively. (D) CV profile at a scanning rate of 0.01 mV s^{-1} between 1.0 and 3.5 V versus Na^+/Na.

at different scanning rates (Figure 4A). The plot of the peak current i_p versus the square root of the scanning rate shows a linear relationship (Figure 4B), indicating good reversibility of the full Na/NYS/S cell.[50,62] As the scanning rate increases, the polarization voltage also increases and the system changes from a reversible to a quasi-reversible state, indicating that electronic conductivity limits the kinetic properties of the S composite.

The *C*-rate performance was tested between 0.01 and 2 C in the full cell (Figure 4C). The applied current at different *C*-rates correlates to the areal current based on the practical S loading in the full cell (shown in Table S4). Starting from 0.01 C, the discharge capacities are between 950 and 970 mAh g_S^{-1}. At a current density of 0.2 and 2 C, the discharge capacities are 790 and 200 mAh g_S^{-1}, which correspond to 82% and 20% of the initial capacity, respectively. After the stepwise *C*-rate test up to 2 C, the discharge capacity increases back to about 880 mAh g_S^{-1} at 0.01 C, corresponding to a retention rate of 91%. The decrease in discharge capacity with the increasing *C*-rate is visualized better in Figure 4D. At a high *C*-rate (high current density), the cathode reaction and the ionic transport in the electrolyte are the limiting processes leading to a significant decrease in capacity. However, 200 mAh g_S^{-1} at 2 C is one of the highest discharge capacities ever reported for an SSB.[63–65]

The cycling performance with the corresponding Coulombic efficiency of the Na/NYS/S full cell is shown in Figure 4E. The initial discharge capacity reaches up to 970 mAh g_S^{-1} at a current density of 0.01 C. The initially chosen higher charging voltage of 3.5 V may induce the decomposition of PEO in the S composite cathode.[66] Therefore, for the long-term test, the cut-off voltage was set to 3.3 V versus Na^+/Na to maintain a stable potential window for the composite cathode. In 150 cycles, the specific discharge capacity of the full cell decreases from 970 to 600 mAh g_S^{-1} (0.25% degradation per cycle based on the initial discharge capacity), showing good cycling stability

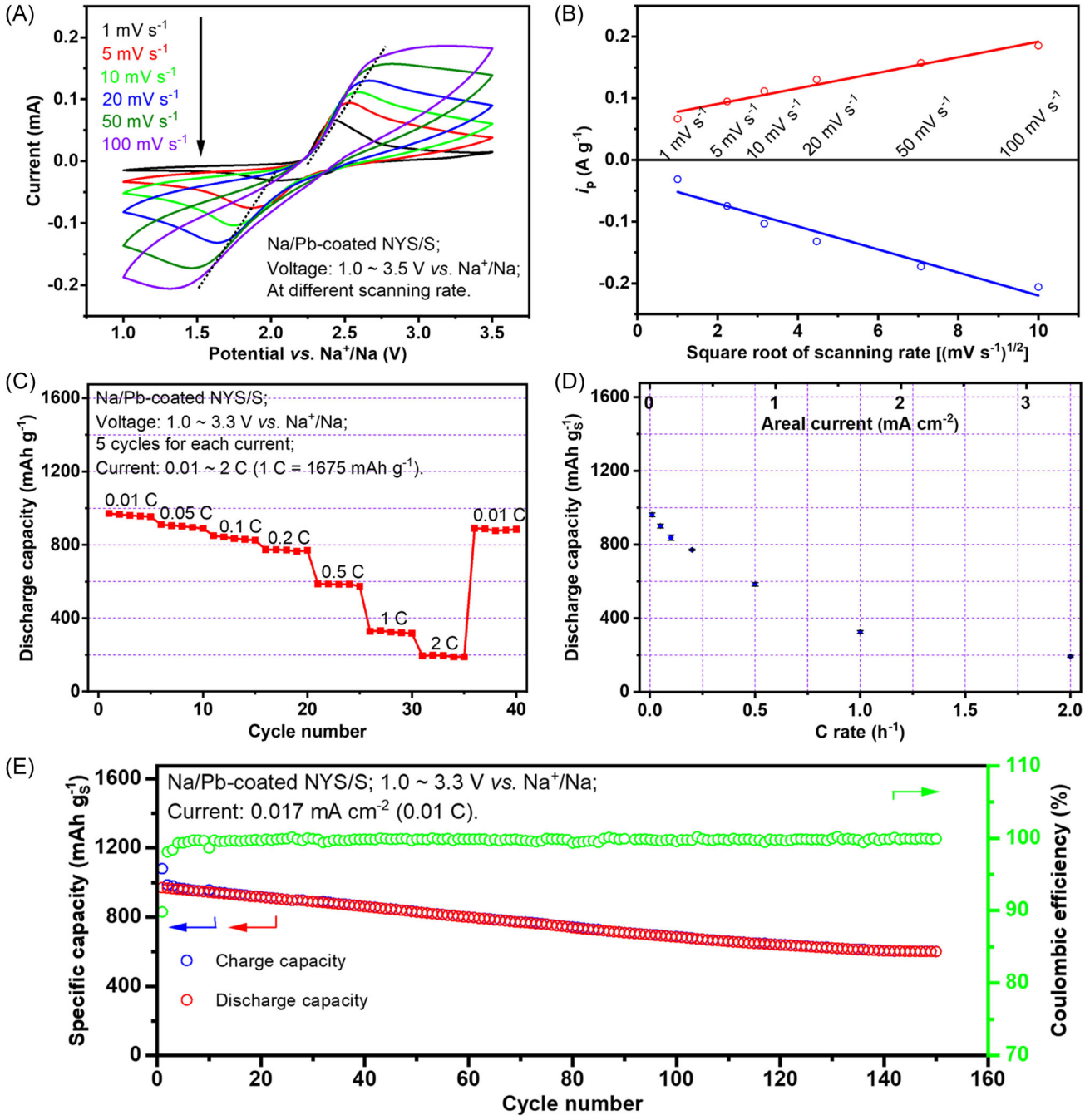

FIGURE 4 Electrochemical performance of Na/NYS/S full cells. (A) CV profiles at different scanning rates from 1 to 100 mV s^{-1} in the range of 1.0–3.5 V versus Na^+/Na. (B) Relationship between peak current i_p and the square root of the scanning rate. (C) *C*-rate performance measurement between 0.01 and 2 C. (D) Change of specific capacity at different *C*-rates and areal current densities. (E) Galvanostatic charge and discharge cycling performance and Coulombic efficiency at a current density of 0.01 C.

due to the capability of the NYS scaffold to effectively prevent the dissolution and shuttling effect of S. The Coulombic efficiency is close to 100%, indicating no significant side reactions in the discharge and charge processes. Nevertheless, a thorough further characterization of the complex composite cathode layer needs to be carried out to identify and mitigate the dominating degradation mechanism.[67]

The photograph of the Na/NYS/S pouch cell (Figure S6) demonstrates its functionality. The capacity of the cell is about 4 mAh and the OCV is ~2.6 V. The light-emitting diode was powered by the pouch cell,

which shows the viability of the full cell operating at RT and without external pressure.

3.4 | Comparison of electrical performance with the reported data

During recent years, a lot of work on SSBs has been conducted based on pellet-type electrolytes.[47] However, full cells using pellets as separators can only demonstrate the generic chemistry or specific electrode modifications under consideration but are far from realistic cell designs and have no perspective with regard to scalable fabrication, adequate specific energy, or cost estimates.[48,68] In the pellet-based SSB cells compared in Figure 5A, the systems $Na/Na_{3.5}Zr_{1.9}Al_{0.1}Si_{2.4}P_{0.6}O_{12}$/S-C,[59] $Na/Na_3PS_{3.85}O_{0.15} + Na_3PS_{3.4}O_{0.6}$/S-C-$Na_3PS_{3.85}O_{0.15}$,[51] Na-Sn-C/$Na_3PS_4$/$Na_3PS_4$-$Na_2S$-C[52], and $Na/Na_{3.4}Zr_2Si_{2.4}P_{0.6}O_{12}$/$Na_3V_2P_3O_{12}$[35] contain a very thick solid electrolyte that is far thicker than both electrodes, especially the cathode. In addition, the areal loading of the active material in the cathode is not high enough. For comparison, the thickness of the inactive SSE is significantly reduced in full cells using tapes. It is impressive that the reported porous $Li_7La_3Zr_2O_{12}$ (LLZO) tape is able to incorporate a loading of up to 5.3 mg cm^{-2} of the cathode material.[69] However, in this case, an ionic liquid-based electrolyte was added to the thick cathode to enhance the ionic conductivity and reduce the interfacial impedance of the cathode. In the porous layer of the NYS scaffold, an areal loading of 1 mg cm^{-2} was realized, which is close to the values in the pellet-based full cells.[52,59] The Ragone plot (Figure 5B) provides a more illustrative comparison of pellet-based and tape-based SSBs as well as batteries with liquid electrolytes. The detailed data are given in Table S5. In pellet-based SSBs using S[51,52,59] and $Na_3V_2P_3O_{12}$[35] as the cathode, the specific power and specific energy are much worse than those of the tape-based batteries and liquid electrolyte batteries.[70] The reason for this is related to the inactive electrolyte, which diminishes the energy density and increases the impedance of the cell. In addition, the thick anodes[35,52] also deteriorate the energy density, because only a small fraction of the thick layer contributes to the cell performance. The established Na/S batteries operating at high temperatures with molten Na and S cannot compete with the tape-based Na/NYS/S cells because of the adoption of the thick β''-Al_2O_3 separator and low utilization rate of the electrodes.[71] It is worth mentioning that the specific energy and specific power of the Na/NYS/S all-solid-state cell are close to or even better than those of the liquid Na/S cell system in the low-current region. In the high current region, its performance is inferior to that of the liquid cell due to insufficient ionic and electronic conductivity and large interfacial impedance. Overall, tape-based all-solid-state Na/NYS/S batteries are anticipated to reach or even outperform conventional liquid batteries and they show potential

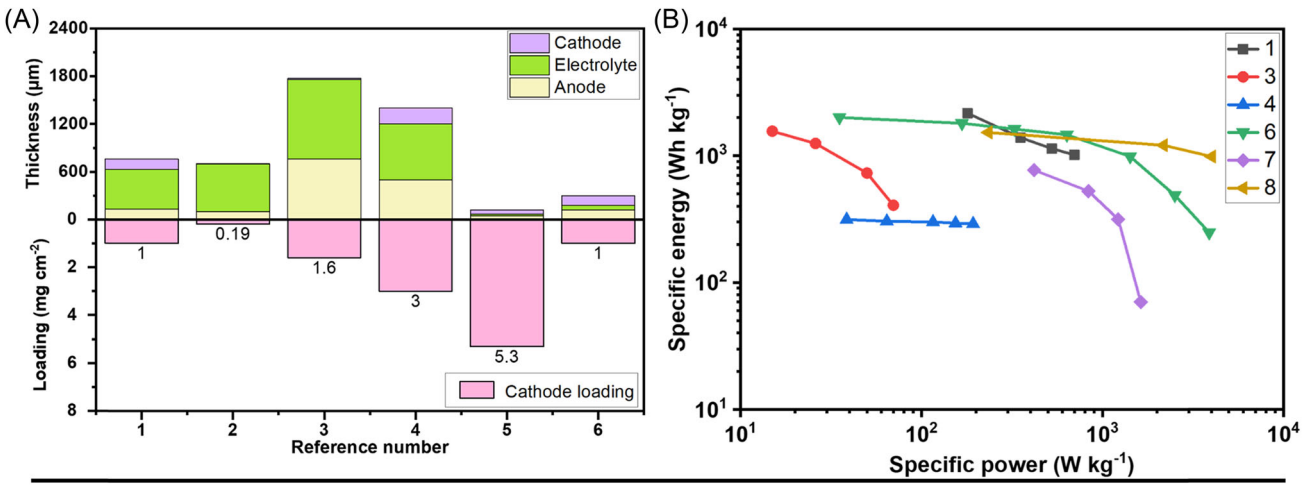

1. $Na/Na_{3.5}Zr_{1.9}Al_{0.1}Si_{2.4}P_{0.6}O_{12}$ (dropped liquid electrolyte)/S-C, pellet;[59]
2. Na/ $Na_3PS_{3.85}O_{0.15}$ + $Na_3PS_{3.4}O_{0.6}$ bi-layer/S-C-$Na_3PS_{3.85}O_{0.15}$, pellet;[51]
3. Na-Sn-C/Na_3PS_4/Na_3PS_4-Na_2S-C, pellet;[52]
4. Na/ $Na_{3.4}Zr_2Si_{2.4}P_{0.6}O_{12}$/ $Na_3V_2P_3O_{12}$, pellet;[35]
5. Li/$Li_7La_3Zr_2O_{12}$/S, tape;[69]
6. Na/NYS/S composite, tape; (This work)
7. Molten Na/β''-Al_2O_3/S, pellet;[71]
8. Na/1 M $NaClO_4$ in PC-EC/S-C, liquid electrolyte.[70]

FIGURE 5 Comparison of different SSB cell architectures (see also Table S5). (A) Layer thicknesses of SSBs and their areal-specific loading of active materials in the cathode. Here mainly sulfur-containing cells were considered. (B) Ragone plot of representative battery cells.

for scalable preparation. Further improvements can be anticipated by increasing the electronic conductivity in the cathode and by rationalizing the degradation behavior.

It is worth noting that the comparisons made above are related to the amount of active materials in the various cell configurations. When the capacity is calculated at the cell level with the experimental data collected here, then the obtained gravimetric and volumetric energy density results in values of 45.57 Wh kg^{-1} and 49.79 Wh L^{-1}, respectively. Details are given in Note S2. These values indicate that further optimizations are necessary to compete with liquid-based batteries. Using calculations on the basis of theoretical capacities, the above values increase to 277 Wh kg^{-1} and 555 Wh L^{-1}, respectively, indicating the high potential of the presented ASS-SMB.

4 | CONCLUSION

In summary, an advanced porous/dense/porous NYS scaffold structure was designed and fabricated by tape casting. The excellent electrochemical performance was demonstrated in Na/NYS/Na symmetric cells and Na/NYS/S full cells. The Na/NYS/Na symmetric cells with a Pb-coated NYS scaffold exhibited an interfacial impedance as low as 25 Ω cm^2 and a CCD of up to 3.0 mA cm^{-2} against the Na metal. The initial discharge capacity in the pressureless Na/NYS/S cells reached up to 970 mAh g_S^{-1} and achieved excellent capacity retention of 600 mAh g_S^{-1} after 150 cycles. The superior performance is attributed to the as-fabricated porous/dense/porous NYS scaffold with a high Na^+ ionic conductivity of 1 mS cm^{-1} at RT, an activation energy as low as 0.29 eV, and a stable electrochemical window up to 8 V (vs. Na^+/Na). Moreover, this particular structural design addresses the issue of vulnerable electrode/electrolyte interfaces that frequently cause challenges in SSBs with sintered composite electrodes. The porous layers provide a host for the active materials and can mitigate the volume changes during charge/discharge processes, thus improving cycling stability. In comparison to SSBs like Na/NaSICON/$Na_3V_2P_3O_{12}$,[35] the infiltration with the polymer/S mixture does not require additional heat treatment to form the active material and provides good contacts during cycling. The NYS scaffold, together with the used cathode formulation, allows operation at RT without external pressure. This work presents a novel paradigm to realize affordable and reliable ASS-SMBs from the perspective of structural manufacturing of ceramic electrolytes.

ACKNOWLEDGMENTS

This work was supported by the China Scholarship Council (CSC, No. 201906200023) and the MatKat Foundation. Aikai Yang, whose CSC grant application is affiliated with Nankai University (Tianjin, China), would like to sincerely thank and express his appreciation to the Key Laboratory of Advanced Energy Materials Chemistry (Ministry of Education) at Nankai University. Partial financial support from the German Federal Ministry of Education and Research (BMBF) within the project "HeNa" (support code 13XP0390B) is also gratefully acknowledged. The authors take responsibility for the content of this publication. The authors acknowledge the technical assistance of Mr. Volker Bader (IEK-1) for the heat treatments. Open Access funding is enabled and organized by Projekt DEAL.

CONFLICT OF INTEREST STATEMENT

The authors declare no conflicts of interest.

ORCID

Aikai Yang http://orcid.org/0000-0002-0906-4719
Frank Tietz http://orcid.org/0000-0002-3724-7627

REFERENCES

1. Dunn B, Kamath H, Tarascon J-M. Electrical energy storage for the grid: a battery of choices. *Science*. 2011;334(6058):928-935.
2. Evarts EC. Lithium batteries: to the limits of lithium. *Nature*. 2015;526(7575):S93-S95.
3. Li M, Lu J. Cobalt in lithium-ion batteries. *Science*. 2020;367(6481):979-980.
4. Yuan Y, Lu J. Demanding energy from carbon. *Carbon Energy*. 2019;1(1):8-12.
5. Or T, Gourley SWD, Kaliyappan K, Yu A, Chen Z. Recycling of mixed cathode lithium-ion batteries for electric vehicles: current status and future outlook. *Carbon Energy*. 2020;2(1):6-43.
6. Zhu Z, Jiang T, Ali M, et al. Rechargeable batteries for grid scale energy storage. *Chem Rev*. 2022;122(22):16610-16751.
7. Yoshino A. The birth of the lithium-ion battery. *Angew Chem Int Ed*. 2012;51(24):5798-5800.
8. Bauer C, Burkhardt S, Dasgupta NP, et al. Charging sustainable batteries. *Nat Sustain*. 2022;5(3):176-178.
9. Hu Y-S. Batteries: getting solid. *Nat Energy*. 2016;1(4):16042.
10. Janek J, Zeier WG. A solid future for battery development. *Nat Energy*. 2016;1(9):16141.
11. Bates AM, Preger Y, Torres-Castro L, Harrison KL, Harris SJ, Hewson J. Are solid-state batteries safer than lithium-ion batteries? *Joule*. 2022;6(4):742-755.
12. Feng J, Gao Z, Sheng L, Hao Z, Wang FR. Progress and perspective of interface design in garnet electrolyte-based all-solid-state batteries. *Carbon Energy*. 2021;3(3):385-409.
13. Su S, Ma J, Zhao L, et al. Progress and perspective of the cathode/electrolyte interface construction in all-solid-state lithium batteries. *Carbon Energy*. 2021;3(6):866-894.

14. Zhou X, Zhang Y, Shen M, et al. A highly stable Li-organic all-solid-state battery based on sulfide electrolytes. *Adv Energy Mater*. 2022;12(14):2103932.
15. Ren Y, Danner T, Moy A, et al. Oxide-based solid-state batteries: a perspective on composite cathode architecture. *Adv Energy Mater*. 2022;13(1):2201939.
16. Hood ZD, Zhu Y, Miara LJ, Chang WS, Simons P, Rupp JLM. A sinter-free future for solid-state battery designs. *Energy Environ Sci*. 2022;15(7):2927-2936.
17. Yung-Fang yu yao Y, Kummer JT. Ion exchange properties of and rates of ionic diffusion in beta-alumina. *J Inorg Nucl Chem*. 1967;29(9):2453-2475.
18. Nakayama M, Kotobuki M, Munakata H, Nogami M, Kanamura K. First-principles density functional calculation of electrochemical stability of fast Li ion conducting garnet-type oxides. *Phys Chem Chem Phys*. 2012;14(28):10008-10014.
19. Kamaya N, Homma K, Yamakawa Y, et al. A lithium superionic conductor. *Nat Mater*. 2011;10(9):682-686.
20. Han F, Zhu Y, He X, Mo Y, Wang C. Electrochemical stability of $Li_{10}GeP_2S_{12}$ and $Li_7La_3Zr_2O_{12}$ solid electrolytes. *Adv Energy Mater*. 2016;6(8):1501590.
21. Huang W, Matsui N, Hori S, et al. Anomalously high ionic conductivity of Li_2SiS_3-type conductors. *J Am Chem Soc*. 2022;144(11):4989-4994.
22. Ahsan MT, Ali Z, Usman M, Hou Y. Unfolding the structural features of NASICON materials for sodium-ion full cells. *Carbon Energy*. 2022;4(5):776-819.
23. Tietz F. Phase relations of NASICON materials and compilation of the quaternary phase diagram Na_2O–P_2O_5–SiO_2–ZrO_2. *AIMS Mater Sci*. 2017;4(6):1305-1318.
24. Ma Q, Ortmann T, Yang A, et al. Enhancing the dendrite tolerance of NaSICON electrolytes by suppressing edge growth of Na electrode along ceramic surface. *Adv Energy Mater*. 2022;12(40):2201680.
25. Hayashi A, Noi K, Sakuda A, Tatsumisago M. Superionic glass-ceramic electrolytes for room-temperature rechargeable sodium batteries. *Nat Commun*. 2012;3:856.
26. Yu X, Xue L, Goodenough JB, Manthiram A. Ambient-temperature all-solid-state sodium batteries with a laminated composite electrolyte. *Adv Funct Mater*. 2020;31(2):2002144.
27. Zhang H, Huang L, Xu H, et al. A polymer electrolyte with a thermally induced interfacial ion-blocking function enables safety-enhanced lithium metal batteries. *eScience*. 2022;2(2):201-208.
28. Tang B, Zhao Y, Wang Z, et al. Ultrathin salt-free polymer-in-ceramic electrolyte for solid-state sodium batteries. *eScience*. 2021;1(2):194-202.
29. Kummer JT, Weber N. A sodium-sulfur secondary battery. *SAE Trans*. 1968;76(2):1003-1007.
30. Kummer JT. β-Alumina electrolytes. *Prog Solid State Chem*. 1972;7:141-175.
31. Coetzer J. A new high energy density battery system. *J Power Sources*. 1986;18(4):377-380.
32. Fertig MP, Skadell K, Schulz M, Dirksen C, Adelhelm P, Stelter M. From high- to low-temperature: the revival of sodium-beta alumina for sodium solid-state batteries. *Batteries Supercaps*. 2021;5(1):e202100131.
33. Zhou C, Bag S, Thangadurai V. Engineering materials for progressive all-solid-state Na batteries. *ACS Energy Lett*. 2018;3(9):2181-2198.
34. Slater MD, Kim D, Lee E, Johnson CS. Sodium-ion batteries. *Adv Funct Mater*. 2013;23(8):947-958.
35. Lan T, Tsai C-L, Tietz F, et al. Room-temperature all-solid-state sodium batteries with robust ceramic interface between rigid electrolyte and electrode materials. *Nano Energy*. 2019;65:104040.
36. Ma Q, Tietz F. Solid-state electrolyte materials for sodium batteries: towards practical applications. *ChemElectroChem*. 2020;7(13):2693-2713.
37. Lu Q, Yang A, Omar A, et al. Recent advances in stabilization of sodium metal anode in contact with organic liquid and solid-state electrolytes. *Energy Technol*. 2022;10(7):2200149.
38. Lu Y, Li L, Zhang Q, Niu Z, Chen J. Electrolyte and interface engineering for solid-state sodium batteries. *Joule*. 2018;2(9):1747-1770.
39. Wang X, Shang Z, Yang A, et al. Combining quinone cathode and ionic liquid electrolyte for organic sodium-ion batteries. *Chem*. 2019;5(2):364-375.
40. Yang A, Wang X, Lu Y, Miao L, Xie W, Chen J. Core-shell structured 1,4-benzoquinone@TiO_2 cathode for lithium batteries. *J Energy Chem*. 2018;27(6):1644-1650.
41. Hüttl J, Cai W, Wagner D, et al. Polarization impedance at the Na–$Na_5YSi_4O_{12}$ interface. *Solid State Ion*. 2022;376:115856.
42. Wang J, Kang Q, Yuan J, et al. Dendrite-free lithium and sodium metal anodes with deep plating/stripping properties for lithium and sodium batteries. *Carbon Energy*. 2021;3(1):153-166.
43. Zhang X, Wang QJ, Peng B, Wu Y. Pressure-driven and creep-enabled interface evolution in sodium metal batteries. *ACS Appl Mater Interfaces*. 2021;13(22):26533-26541.
44. Shen X, Zhang R, Shi P, Chen X, Zhang Q. How does external pressure shape Li dendrites in Li metal batteries? *Adv Energy Mater*. 2021;11(10):2003416.
45. Tsai C-L, Lan T, Dellen C, et al. Dendrite-tolerant all-solid-state sodium batteries and an important mechanism of metal self-diffusion. *J Power Sources*. 2020;476:228666.
46. Yang A, Ye R, Li X, et al. Fabrication of thin sheets of the sodium superionic conductor $Na_5YSi_4O_{12}$ with tape casting. *Chem Eng J*. 2022;435(Part 1):134774.
47. Albertus P, Anandan V, Ban C, et al. Challenges for and pathways toward Li-metal-based all-solid-state batteries. *ACS Energy Lett*. 2021;6(4):1399-1404.
48. Balaish M, Gonzalez-Rosillo JC, Kim KJ, Zhu Y, Hood ZD, Rupp JLM. Processing thin but robust electrolytes for solid-state batteries. *Nat Energy*. 2021;6(3):227-239.
49. Zhao M, Li X-Y, Chen X, et al. Promoting the sulfur redox kinetics by mixed organodiselenides in high-energy-density lithium-sulfur batteries. *eScience*. 2021;1(1):44-52.
50. Wu J, Tian Y, Gao Y, et al. Rational electrolyte design toward cyclability remedy for room-temperature sodium-sulfur batteries. *Angew Chem Int Ed*. 2022;61(30):e202205416.
51. Chi X, Zhang Y, Hao F, et al. An electrochemically stable homogeneous glassy electrolyte formed at room temperature for all-solid-state sodium batteries. *Nat Commun*. 2022;13:2854.
52. Yue J, Han F, Fan X, et al. High-performance all-inorganic solid-state sodium-sulfur battery. *ACS Nano*. 2017;11(5):4885-4891.

53. Yue X-Y, Zhang J, Bao J, et al. Sputtered MoN nanolayer as a multifunctional polysulfide catalyst for high-performance lithium–sulfur batteries. *eScience*. 2022;2(3):329-338.
54. Huang C-J, Cheng J-H, Su W-N, et al. Origin of shuttle-free sulfurized polyacrylonitrile in lithium-sulfur batteries. *J Power Sources*. 2021;492:229508.
55. Weret MA, Su WN, Hwang BJ. Strategies towards high performance lithium–sulfur batteries. *Batteries Supercaps*. 2022;5(8):e202200059.
56. Chang H-J, Lu X, Bonnett JF, et al. Decorating β''-alumina solid-state electrolytes with micron Pb spherical particles for improving Na wettability at lower temperatures. *J Mater Chem A*. 2018;6(40):19703-19711.
57. Sun G, Yang X, Chen N, et al. $Na_5YSi_4O_{12}$: a sodium superionic conductor for ultrastable quasi-solid-state sodium-ion batteries. *Energy Storage Mater*. 2021;41:196-202.
58. Cai S, Tian H, Liu J, et al. Tuning $Na_3Hf_2Si_2PO_{12}$ electrolyte surfaces by metal coating for high-rate and long cycle life solid-state sodium ion batteries. *J Mater Chem A*. 2022;10(3):1284-1289.
59. Lu L, Lu Y, Alonso JA, et al. A monolithic solid-state sodium-sulfur battery with Al-doped $Na_{3.4}Zr_2(Si_{0.8}P_{0.2}O_4)_3$ electrolyte. *ACS Appl Mater Interfaces*. 2021;13(36):42927-42934.
60. An T, Jia H, Peng L, Xie J. Material and interfacial modification toward a stable room-temperature solid-state Na–S battery. *ACS Appl Mater Interfaces*. 2020;12(18):20563-20569.
61. Wang Y-X, Zhang B, Lai W, et al. Room-temperature sodium-sulfur batteries: a comprehensive review on research progress and cell chemistry. *Adv Energy Mater*. 2017;7(24):1602829.
62. Zhang S, Yao Y, Yu Y. Frontiers for room-temperature sodium-sulfur batteries. *ACS Energy Lett*. 2021;6(2):529-536.
63. Zhou W, Li Y, Xin S, Goodenough JB. Rechargeable sodium all-solid-state battery. *ACS Cent Sci*. 2017;3(1):52-57.
64. Liu L, Qi X, Ma Q, et al. Toothpaste-like electrode: a novel approach to optimize the interface for solid-state sodium-ion batteries with ultralong cycle life. *ACS Appl Mater Interfaces*. 2016;8(48):32631-32636.
65. Yang J, Liu G, Avdeev M, et al. Ultrastable all-solid-state sodium rechargeable batteries. *ACS Energy Lett*. 2020;5(9):2835-2841.
66. Zhou W, Gao H, Goodenough JB. Low-cost hollow mesoporous polymer spheres and all-solid-state lithium, sodium batteries. *Adv Energy Mater*. 2016;6(1):1501802.
67. Zhang S, Zhao K, Zhu T, Li J. Electrochemomechanical degradation of high-capacity battery electrode materials. *Prog Mater Sci*. 2017;89:479-521.
68. Wang MJ, Kazyak E, Dasgupta NP, Sakamoto J. Transitioning solid-state batteries from lab to market: linking electro-chemo-mechanics with practical considerations. *Joule*. 2021;5(6):1371-1390.
69. Hitz GT, McOwen DW, Zhang L, et al. High-rate lithium cycling in a scalable trilayer Li-garnet-electrolyte architecture. *Mater Today*. 2019;22:50-57.
70. Xin S, Yin YX, Guo YG, Wan LJ. A high-energy room-temperature sodium-sulfur battery. *Adv Mater*. 2014;26(8):1261-1265.
71. Li MM, Lu X, Zhan X, et al. High performance sodium-sulfur batteries at low temperature enabled by superior molten Na wettability. *Chem Commun*. 2021;57(1):45-48.

SUPPORTING INFORMATION

Additional supporting information can be found online in the Supporting Information section at the end of this article.

How to cite this article: Yang A, Ye R, Song H, et al. Pressureless all-solid-state Na/S batteries with self-supporting $Na_5YSi_4O_{12}$ scaffolds. *Carbon Energy*. 2023;5:e371. doi:10.1002/cey2.371